

Self-Induced Dual-Layered Solid Electrolyte Interphase with High Toughness and High Ionic Conductivity for Ultra-Stable Lithium Metal Batteries

Xin Hu, Yitian Ma, Ji Qian,* Wenjie Qu, Yu Li, Rui Luo, Huirong Wang, Anbin Zhou, Yi Chen, Keqing Shi, Li Li, Feng Wu, and Renjie Chen*

Lithium (Li) metal is considered as one of the most promising candidates of anode material for high-specific-energy batteries, while irreversible chemical reactions always occur on the Li surface to continuously consume active Li, electrolyte. Solid electrolyte interphase (SEI) layer has been regarded as the key component in protecting Li metal anode. Herein, a controllable dual-layered SEI for Li metal anode in a scalable, low-loss manner is constructed. The SEI is self-induced by the predeposited LiAlO_2 (LAO) layer during the initial cycles, in which the outer organic layer is produced due to the electrons tunneling through LAO, resulting in the reduction of electrolyte. The robust inner LAO layer can promote uniform Li deposition owing to its favorable mechanical strength and ionic conductivity, and the outer organic layer can further improve the stability of SEI. Benefiting from the remarkable effects of this dual-layered SEI, enhanced electrochemical performance of the LAO–Li anode is achieved. Additionally, a large-size LAO–Li sample can be easily obtained, and the preparation of the modified Li metal anode shows huge potential for large-scale production. This work highlights the tremendous potential of this self-induced dual-layered SEI for the commercialization of Li metal anode.

1. Introduction

Due to the rapid development of portable and flexible electronic devices, lithium-ion batteries (LIBs) gradually cannot meet the ever-increasing demands of powerful energy storage devices. To meet these growing demands, quite a few works have been reported to develop new battery systems and materials.^[1] Li metal is considered as one of the most promising candidates of anode material for high-specific-energy batteries because of its high theoretical capacity of 3860 mAh g^{-1} and the lowest electrochemical potential of -3.04 V (vs. standard hydrogen electrode).^[2] Particularly, in the next-generation batteries with high energy density, like Li–S battery with theoretical specific energy of $\approx 2567 \text{ Wh kg}^{-1}$ and Li–air battery with a theoretical specific energy of $\approx 3505 \text{ Wh kg}^{-1}$, Li metal anode is a vital and irreplaceable component.^[3] However, blamed for its low electrochemical potential, irreversible chemical reactions

always occur on the Li surface in almost all kinds of liquid electrolytes, which will continuously consume active Li and electrolytes.^[4]

Solid electrolyte interphase (SEI) layer, produced from the reaction between Li metal and electrolyte, has been regarded as the key component in protecting the Li metal anode. Naturally formed SEI film on Li metal anode after cycling is heterogenous in chemical components and physical structures, mechanically weak, and fragile, which makes it difficult to adapt to the volume changes during electrochemical cycling processes. As a result, the repeated rupture and regeneration of SEI occurs, which results in two main problems (upper in Figure 1). The growth of Li dendrites may penetrate the separator and cause a short circuit in the cell, resulting in massive thermal runaway and even causing an explosion. Additionally, the rapid consumption of electrolyte and active Li, generating large amounts of “dead Li”, leading to the performance degradation or even cell failure. Recently, various strategies to engineer the interfacial layer on Li anode have been carried out to alleviate these problems, such as covering protective layer of inorganic Al_2O_3 ,^[5] LiF ,^[6] carbon nanomaterials,^[7] MOFs,^[8] composite layer,^[9] or constructing 3D alloy structures^[10] on Li surface to block the side reactions of

X. Hu, J. Qian, Y. Li, R. Luo, H. Wang, A. Zhou, Y. Chen, L. Li, F. Wu, R. Chen

Beijing Key Laboratory of Environmental Science and Engineering
School of Material Science and Engineering
Beijing Institute of Technology
Beijing 100081, P. R. China
E-mail: jiqian@bit.edu.cn; chenrj@bit.edu.cn

Y. Ma

School of Materials
Xi'an University of Science and Technology
Xi'an 710054, China

J. Qian, K. Shi, L. Li, F. Wu, R. Chen
Advanced Technology Research Institute
Beijing Institute of Technology
Jinan 250300, China

W. Qu

Shanghai Institute of Space Power-Sources
Shanghai 200245, China

L. Li, F. Wu, R. Chen
Collaborative Innovation Center of Electric Vehicles in Beijing
Beijing 100081, China

The ORCID identification number(s) for the author(s) of this article can be found under <https://doi.org/10.1002/adma.202303710>

DOI: 10.1002/adma.202303710

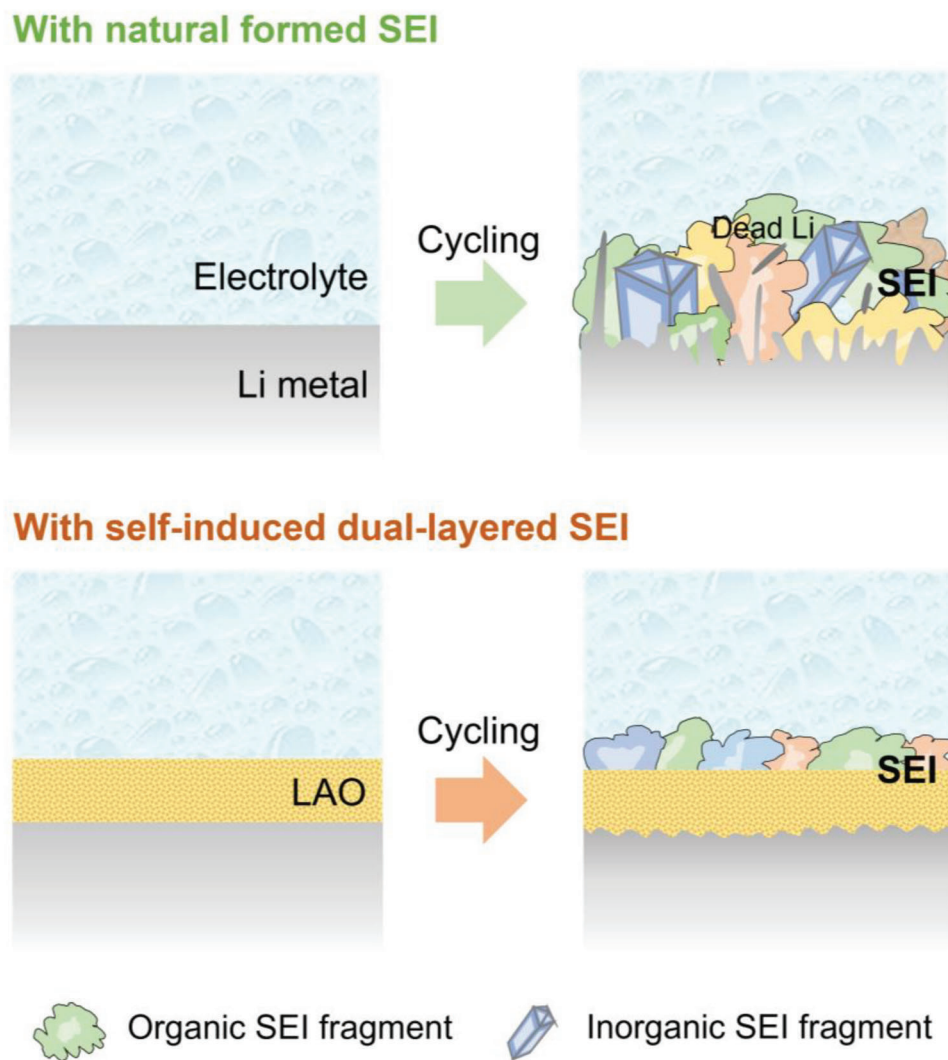


Figure 1. Schematics illustrating the natural SEI (upper) and the target dual-layer SEI (bottom) formed on the Li metal anode, and the corresponding morphology changes of Li metal anodes with different SEI after cycling.

electrodes corrosion or enhance interfacial electron transport; adding additives to the electrolyte,^[11] or designing a highly concentrated electrolyte system^[12] to improve the SEI structure of the Li anode surface and enhance the performance of LMBs. Therefore, the construction of a stable and uniform SEI layer on the Li metal surface is essential for high-performance LMBs.^[13] The dual-layered SEI with an organic layer on the top and inorganic layer near the Li surface has been demonstrated as an ideal structured SEI for Li metal anode.^[14] The outer organic layer can facilitate rapid Li-ion diffusion and achieve flexibility stress to release stress during Li plating/stripping. Further, the inorganic layer can block the electrons transfer and suppress the side reaction with electrolyte and the growth of Li dendrite.^[15] However, constructing controllable dual-layered SEI in a scalable and low-loss manner is still an important issue to improve the performance of Li metal anode.

Herein, we demonstrate a self-induced dual-layered SEI with high toughness and high ionic conductivity for ultra-stable lithium metal batteries. We directly pre-deposit an ultra-thin

LiAlO₂ (LAO) film on the surface of Li metal via radio-frequency magnetron sputtering method as a robust and Li-ion conductive inorganic layer. Subsequently, the outer organic layer will be produced during the initial electrochemical cycles due to the electrons tunneling through LAO, resulting in the reduction of electrolytes and the formation of the outer organic layer. As a result, the unique self-induced dual-layered SEI could form on the Li metal anode. The inner LAO layer produced via magnetron sputtering on the Li surface is highly uniform and tight-contacted with the Li metal,^[16] which is superior to the previously reported nonuniform and discontinuous lithium alumina oxide compounds obtained in lithiation reaction between Al₂O₃ modifier and Li metal anode.^[17] The robust LAO layer can effectively suppress the Li dendrite growth and lead to uniform Li deposition because of its favorable mechanical strength and ionic conductivity. Meanwhile, the outer organic layer can further improve the stability of the interphase between the Li metal anode and electrolyte (bottom in Figure 1). Additionally, the fabrication of the modified Li metal anode with self-induced dual-layered SEI

is highly scalable. Benefiting from the remarkable effects of the dual-layered SEI, the electrochemical performance and cycling life of the Li symmetric cell, as well as various kinds of full cells, containing the modified Li metal anode is greatly improved.

2. Results and Discussion

The thickness of the LAO film is a key factor to affect the performance of the modified Li (LAO-Li) anode. To determine the appropriate thickness of the LAO film for the fabrication of LAO-Li anode, we prepare the LAO films with different sputtering times (1 min, 2 min, and 5 min) and evaluate the effects of LAO film's thickness on the Li⁺ ion transport. The thicknesses of the LAO films are estimated to be ≈ 8.1 nm, ≈ 16.2 nm, and ≈ 40.5 nm based on the deposit rate of 8.1 nm min^{-1} . The determination of deposit rate is detailed in Figure S1, Supporting Information. We sputtered the LAO layer onto the commercial Celgard 2300 separator and assembled a blocking resistance system with two stainless steel (SS) slices and the modified membrane with electrolyte (MME), as shown in Figure 2a.^[10e] The Li⁺ ionic conductivity of the MME is evaluated with the AC impedance measurements. Nyquist plots of the cells containing the LAO films prepared with different sputtering times are shown in Figure 2b. The resistance (R_{MME}) values can be determined by reading the X-intercept from the Nyquist plots and the corresponding ionic conductivity values are calculated with the equation

$$\sigma = d / (R_{\text{MME}} \times A) \quad (1)$$

where σ , d , A , and R_{MME} are the ionic conductivity, thickness, area, and resistance of the MME.

Due to the thickness of the LAO film being nanoscale, it is negligible comparing to the thickness of the MME, and the average value of d is $28 \text{ }\mu\text{m}$. The contact area between stainless steel and membrane, namely A , is 0.95 cm^2 . The conductivity values of these membranes shown in Figure 2c are calculated with the aforementioned Equation (1) and the parameters are listed in Table S1, Supporting Information. By contrast, the conductivity of the MMEs with the LAO film is higher than that of the unmodified MME, which confirms that the LAO film plays an effective role in enhancing the mobility of lithium ions between electrodes and electrolyte, proving that LAO film is an ideal candidate to construct the artificial SEI. Meanwhile, the different exchange current densities are compared via the Tafel profiles, which also confirm the higher charge-transfer kinetic and faster Li ion transport of LAO films than that of the unmodified Li surface (Figure S2, Supporting Information). Moreover, the membrane with the 2 min-sputtering LAO film shows the highest conductivity. We speculate the reason is that too short sputtering time may cause the nonuniform cover layer and disparity of resistance at local areas, and too long sputtering time will lead to an extremely thick cover layer and impede the charge transfer at the electrolyte/electrode interface. Therefore, we use the magnetron sputtering time of 2 min to prepare all LAO-Li samples hereafter.

Scanning electron microscopy (SEM) images of the unmodified Li (Figure 2d) and LAO-Li (Figure 2e) anodes reveal that the texture of pristine lithium foil is concealed by a homogeneous LAO coating layer after the magnetron sputtering treatment. The

uniform distribution of LAO is further confirmed by the energy-dispersive X-ray spectroscopy (EDS) elemental mapping of Al and O in Figure 2f. To suppress the growth of lithium dendrite for protection, high mechanical strength is vital for the inorganic layer of the artificial SEI film.^[18] To evaluate the mechanical strength of the LAO layer, we further carried out the atom force microscope (AFM) measurement to test the Young's modulus of the LAO layer deposited on the silicon wafer. Figure 2g shows the morphology of the LAO film probed by AFM and Figure 2h shows the corresponding modulus distribution of the LAO film. Through the observation of the topography image of the surface, we can confirm that there has no obvious fluctuation of LAO film, indicating that flat LAO film can be formed via the magnetron sputtering method. Further, the quantitative distribution of the Young's modulus of the LAO film (Figure 2h) shows that the modulus mainly distributes within the range of 3–16 GPa with an average Young's modulus of 5.88 GPa (Figure 2i). It has been reported that the maximum stresses of lithium dendrite growth vary from tens of MPa to over 130 MPa^[19] and the elastic modulus of 5–7 GPa is required to inhibit macroscopic dendrite formation.^[20] Therefore, we can confirm that the robust mechanical property of LAO film is tough enough to restrain the lithium dendrite growth.^[10d,19]

Owing to the tightly attached LAO layer with Li metal surface, the LAO-Li can effectively suppress the side reactions with both air and electrolyte in spite of the high reactivity of Li metal. We exposed the unmodified Li and LAO-Li to air for 2 days (Figure 2j and Figure S3, Supporting Information) and we noticed that the surface of the unmodified Li got dark black and the edge curled up, as a result of the reactions with air that producing impurities of Li₃N and LiOH. By contrast, the LAO-Li showed partially original brilliant metal, indicating that the LAO layer could effectively protect lithium metal from the oxidative atmosphere. Similarly, the LAO-Li exhibits good stability against electrolyte. We assembled the symmetric cells with the unmodified Li (Figure 2k) or LAO-Li (Figure 2l) electrodes and performed the AC impedance measurements to obtain the resistances of the cells after different resting times (Figure 2m). It is observed that the initial resistance values of the cells are both at $\approx 95 \text{ }\Omega$, indicating the LAO layer shows negligible effect on the resistance of the cell. Nonetheless, for the cell with the unmodified Li electrodes, the resistance of the cell distinctly increases to $\approx 180 \text{ }\Omega$ after resting for 36 h. On the contrary, the resistance of the cell with LAO-Li electrodes remains at $130 \text{ }\Omega$ after resting. These results suggest that the LAO layer avails the interfacial stability between the Li anodes and electrolyte and it can completely satisfy the request for constructing the dual-layer SEI with great effects.

To confirm the dual-layered features of the SEI layer formed on LAO-Li anode, we carried out the X-ray photoelectron spectroscopy (XPS) depth profiling experiment on the LAO-Li anode after 3 cycles, as well as the unmodified Li anode for comparison. The XPS depth profiles were collected and the etching rate was standardized by Si samples to be 5 nm min^{-1} . For the unmodified Li anode, the elements content of the natural SEI was relatively constant with the etching depth increasing up to 45 nm, as shown in Figure 3a. According to the XPS peak fitting results shown in Figure S4, Supporting Information, the natural SEI formed on the unmodified Li anode was mainly composed of the organic

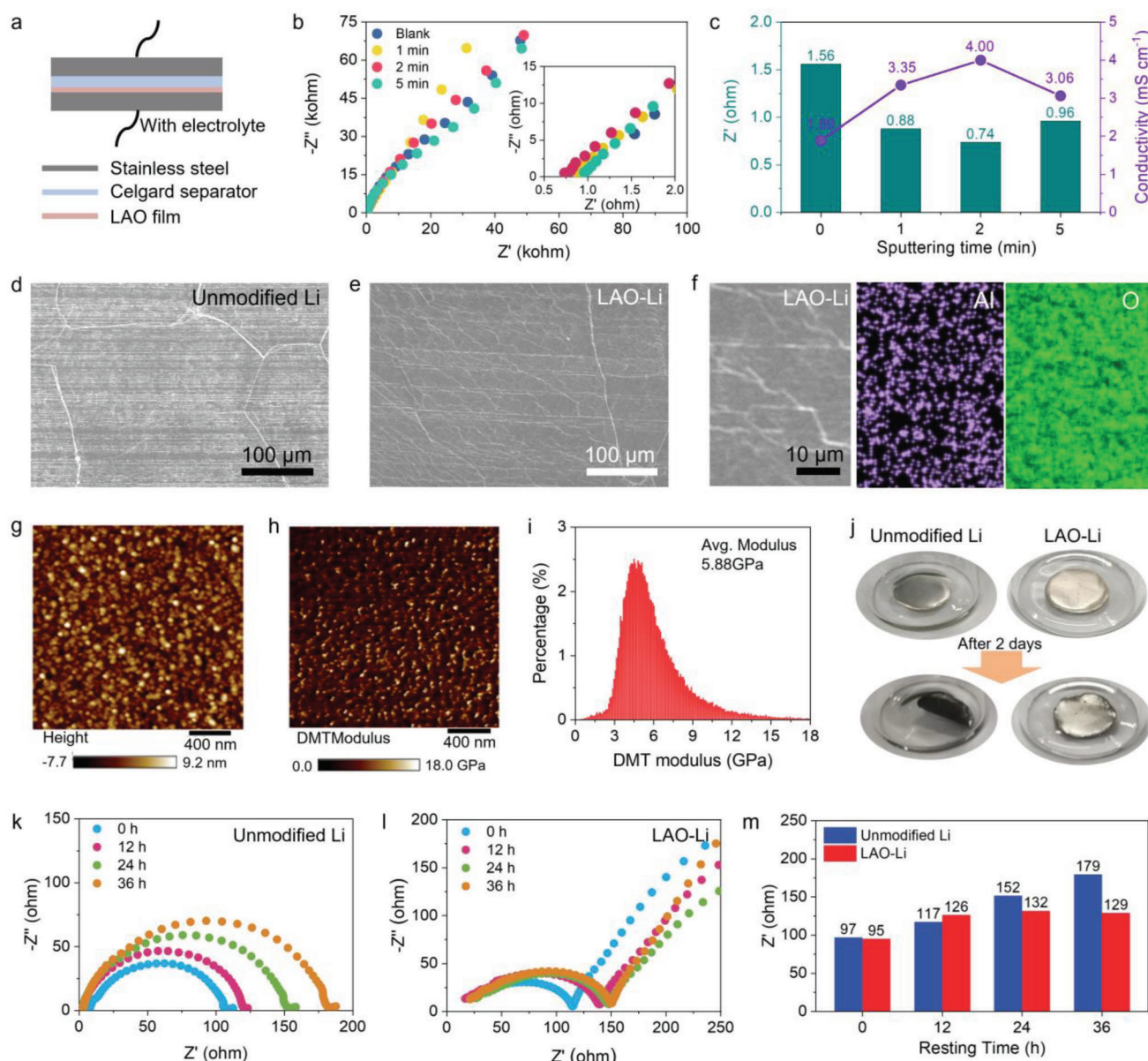


Figure 2. a) Schematics of the cell used to evaluate the Li ionic conductivity of the LAO films. b) Nyquist plots of the cells containing the LAO films prepared with different sputtering times and c) the corresponding resistance and ionic conductivity values obtained from the Nyquist plots in (b). d,e) SEM image of the d) unmodified Li and e) LAO-Li electrodes. f) EDS elemental mapping of LAO-Li anode. g) The AFM topography image of the LAO-Li anode and h) the corresponding distribution of the Young's modulus. i) The quantitative distribution of the Young's modulus of the LAO film. j) Photo images of the unmodified Li and LAO-Li anodes before and after exposure to air for 2 days. k-m) Nyquist plots of the symmetric cells with k) unmodified Li or l) LAO-Li electrodes during the resting process of 36 h and m) the corresponding resistance values obtained from the Nyquist plots in (k) and (l).

component of ROCO_2Li and ROLi with a small amount of inorganic component of Li_2CO_3 and Li_3N , which is consistent with the Mosaic-type SEI that has been reported in the literature.^[21] In contrast, the SEI on LAO-Li anode exhibits an obvious dual-layer structure. As shown in Figure 3b,c, along with the increasing etching depth, the contents of N and C sharply decrease and the C species almost disappear within the depth of 20 nm, indicating the presence of the organic layer. It also confirms that much fewer electrolyte and active Li are consumed to construct the SEI on the LAO-Li anode during cycling, comparing to those

on the unmodified Li anode with the SEI thicker than 45 nm. With further etching, the components of the inner SEI layer are mainly Li, Al, and O atoms and their corresponding contents remain stable. The Al 2p, Li 1s, and O 1s XPS spectra in Figure 3c and Figure S5, Supporting Information, further confirm that the inner inorganic layer can be assigned to the LAO-based inorganic layer. These XPS results confirm the in-situ construction of a superior dual-layers SEI on the LAO-Li anode upon cycling, which provides benefits to the interface stability of Li metal anode.

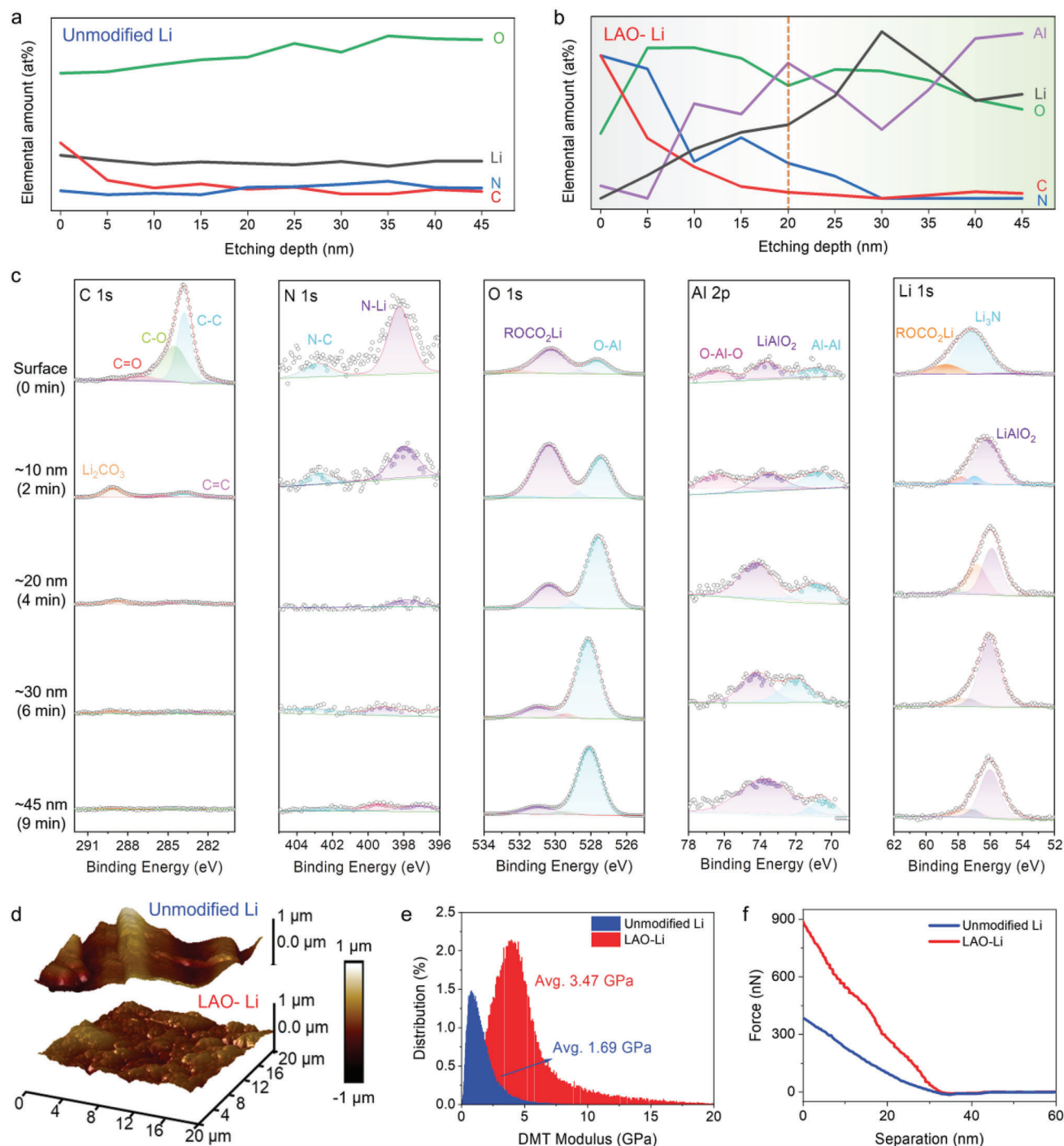


Figure 3. The XPS depth profiles of a) the unmodified Li and b) the LAO-Li anodes after 3 cycles. c) C 1s, N 1s, O 1s, Al 2p, and Li 1s XPS spectra of the LAO-Li anodes after 3 cycles at different etching depths. d) The AFM topography images of the unmodified Li and the LAO-Li anodes after 3 cycles. e) The quantitative distribution of the Young's modulus and f) the Force-Separation curves of the SEI layers on the unmodified Li and the LAO-Li anodes after 3 cycles.

Furthermore, the dual-layer SEI structure was resolved by time-of-flight secondary ion mass spectrometry (ToF-SIMS). The Al and CH₃O⁻, as the characteristic ionic fragments of LAO and organic components respectively, were analyzed (Figure S6, Supporting Information). CH₃O⁻ is abundant in both surfaces of the

LAO-Li and unmodified Li anodes, implying the organic components in the formed SEI resulting from the decomposition of electrolyte. The three-dimensional (3D) structure of dual-layer SEI was further resolved by depth sputtering analysis. As sputtering depth increases, distinct layers of CH₃O⁻ and Al fragments

were sequentially detected in the SEI of LAO-Li, proving its dual-layer structure. In contrast, CH_3O^- fragments are inhomogeneously distributed along the depth, indicating the nonuniform Li deposition and the uneven SEI layer formed after cycling. Additionally, the Li deposition on LAO modified Cu grid was also observed by cryo-transmission electron microscopy (cryo-TEM) to analyze the SEI structure. As shown in Figure S7, Supporting Information, abundant C, O, and Al atoms were observed through the EDS combined with cryo-TEM which represents organic layer (C and O) and inorganic layer (Al and O) in a dual-layer SEI structure. From the above results, we infer that Li deposits below the LAO layer and in situ forms a dual-layer SEI.

The AFM topography images reveal the uneven surface of the unmodified Li anode (top in Figure 3d), while a good surface uniformity is observed for the LAO-Li anode (bottom in Figure 3d). The distribution of Young's modulus of the Li deposition on the unmodified Li is in the range of ≈ 0 to 3 GPa with an average of 1.69 GPa, while for the Li anode with LAO, the Young's modulus distributes in a range of ≈ 1 to 7 GPa with an average of 3.47 GPa (Figure 3e). Further, we take out retraced Force-Separation curve by AFM (Figure 3f), and the divergent slopes of curves were consistent with the Young's modulus in Figure 3e, confirming the denser Li deposition under the regulation of LAO film.

To visually observe and compare the Li deposition behaviors on the unmodified Li and LAO-Li anodes, we set up a sealed transparent Li-Li symmetric cell with a glass window to monitor the surface changes on these two different anodes with an optical microscope equipped with a digital camera (Figure S8, Supporting Information). Li is electroplated onto the anodes at a current density of 1 mA cm^{-2} for 30 min (i.e., 0.5 mAh cm^{-2}). During the Li plating process on the unmodified Li anode, uncontrolled lithium dendrite growth is observed (Figure 4a and Figure S9, Supporting Information). By contrast, the uniform Li deposition is achieved on the surface of LAO-Li without obvious Li dendrite growth (Figure 4b). This contrast difference in morphology of Li deposition can be proved by the 3D optical profilometry images of the anodes after 30 min of Li plating. The unmodified Li anode shows the inhomogeneous Li deposition with areas of Li dendrites growing to a height of $\approx 90 \mu\text{m}$ (Figure 4c), while much more flat Li deposition is observed on the LAO-Li anode (Figure 4d).

To investigate the protective effect of the LAO-based self-induced dual-layered SEI for Li metal anode during cycling, the symmetric cells were assembled using a commercial ether-based electrolyte for Li plating/stripping measurement. The rate performance of the symmetric cell is shown in Figure 4e, and the overpotential of the symmetric cell with unmodified Li anodes increases much more dramatically than that of the cell with LAO-Li anode at stepwise increased current densities. As the voltage profiles illustrated in Figure S10, Supporting Information, the voltage polarization of the LAO-Li anode presents as 15, 25, 40, and 53 mV at 1, 2, 4, and 8 mA cm^{-2} , respectively, while that of the unmodified Li anode is 19, 32, 48, and 94 mV at the same current density. When the current density decreases back to 1 mA cm^{-2} , the voltage polarization of the LAO-Li anode is 14 mV, much lower than that of the unmodified Li anode (23 mV). These data suggest lower interface resistance for the LAO-Li anode than that for the unmodified Li anode. Long-term cycling stability of the LAO-Li anode is further demonstrated at a current density

of 1 mA cm^{-2} and an areal capacity of 1 mAh cm^{-2} (Figure 4f and Figure S11, Supporting Information). The LAO-Li anode exhibits excellent stability and maintains a low overpotential up to 1900 h. Compared with the performance of Li metal anode reported in previous papers (Table S2, Supporting Information), LAO-Li anode exhibits superior performance and shows impressive potential for practical application. By contrast, unmodified Li anode has a much larger overpotential and shows a sudden voltage drop at 470 h because of the short-circuiting. We also conducted the Coulombic efficiency (CE) measurements to quantitatively evaluate the protective effect of self-induced dual-layered SEI for Li depositing. The Cu foil modified by LAO layer was tested using Li||Cu half-cell setup at the current density of 1 mA cm^{-2} and areal capacity of 1 mAh cm^{-2} . As shown in Figure S12a, Supporting Information, Li||LAO-Cu exhibits more stable cycling performance. The benefit of self-induced dual-layered SEI was further validated by Aurbach CE measurements,^[22] in which LAO-Cu shows a higher average CE of 98.4% than that of 93.5% for unmodified Cu (Figure S12b, Supporting Information).

To further confirm the protection for Li metal anode with the dual-layered SEI, we disassembled the cells after 100 cycles, washed and dried the Li anodes in an inert atmosphere, and then observed the morphology changes of these cycled Li anodes. As shown in Figure 4g, the unmodified Li anode shows large amounts of lithium dendrites and severe pulverization. Notably, the surface of LAO-Li presents integrally flat morphology with no obvious lithium dendrite growth and powdering phenomenon demonstrating the remarkable protection role of the LAO-based SEI layer (Figure 4h).

We then evaluate the performance of LAO-Li anode in full cells with sulfur cathode, $\text{Li}_4\text{Ti}_5\text{O}_{12}$ cathode (LTO), LiFePO_4 cathode (LFP), and Ni-rich $\text{LiNi}_{0.8}\text{Co}_{0.1}\text{Mn}_{0.1}\text{O}_2$ cathode (NCM811). Additionally, we assembled the cells with unmodified Li anodes for comparison. For the Li-S cells, the sulfur loading within the cathode is $\approx 3 \text{ mg cm}^{-2}$. As shown in Figure 5a, the cell with the LAO-Li anode presents better rate performance comparing to the cell with an unmodified Li anode, especially at high rate of 2C ($1\text{C} = 1200 \text{ mA g}^{-1}$). The LAO-Li||S cell exhibits a specific capacity of 1050 mAh g^{-1} at 0.1 C with a remaining capacity of 600 mAh g^{-1} at 2C. By contrast, the unmodified Li||S cell only shows a much lower capacity of 200 mAh g^{-1} remained at 2C. Moreover, the increase of voltage polarization at higher rates of the unmodified Li||S cell is more severe than that of LAO-Li||S cell (Figure S13, Supporting Information). The LAO-Li||S cell also shows a much better cycling performance (Figure 5b) with an initial capacity of 761 mAh g^{-1} and a remaining capacity of 603 mAh g^{-1} after 150 cycles with stable CEs and inconspicuous increasing of polarization or overpotential (Figure S14, Supporting Information), while the unmodified Li||S cell only shows a remained capacity of only 331 mAh g^{-1} after cycling, which proves the superiority of LAO-Li anode for Li-S batteries with higher discharge capacity and excellent cycling stability. Even when the N/P ratio decreased to ≈ 1.9 with a $50 \mu\text{m}$ LAO-Li anode used, good cycling performance of the LAO-Li||S cell is still maintained with more limited Li source (Figure S15, Supporting Information). The Li-LTO cells with the LAO-Li anode also exhibit superior electrochemical performance to the cells with the unmodified Li anode. The mass loading of active materials in LTO cathode is $\approx 7.3 \text{ mg cm}^{-2}$. As the rate performance shown in Figures 5c and S16,

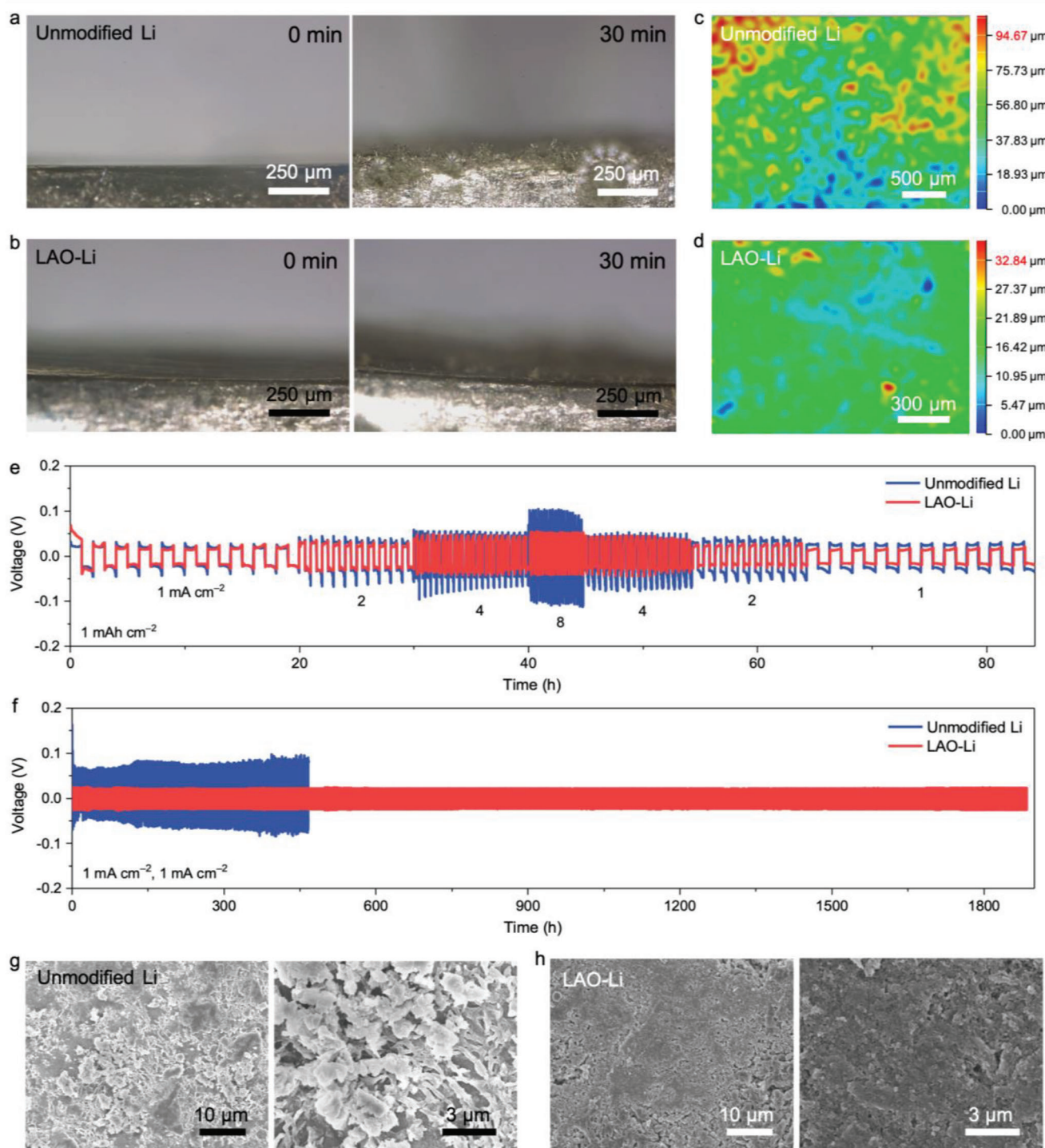


Figure 4. Operando optical microscopy images of the cross-section of a) unmodified Li and b) LAO-Li anodes in a symmetric transparent cell before and after Li depositing for 30 min at a current density of 1 mA cm^{-2} , and c,d) their corresponding 3D optical profilometry images after Li plating for 30 min. e) Li stripping and plating profiles in symmetric cells with the unmodified Li or LAO-Li anodes at stepwise increased current densities from 1 mA cm^{-2} to 8 mA cm^{-2} and then decreased to 1 mA cm^{-2} . f) Long-term cycling stability of the symmetric cells with the unmodified Li or LAO-Li anodes at a current density of 1 mA cm^{-2} and an areal capacity of 1 mAh cm^{-2} . SEM images of the g) unmodified Li and h) LAO-Li anodes after 100 cycles at a current density of 1 mA cm^{-2} and an areal capacity of 1 mAh cm^{-2} .

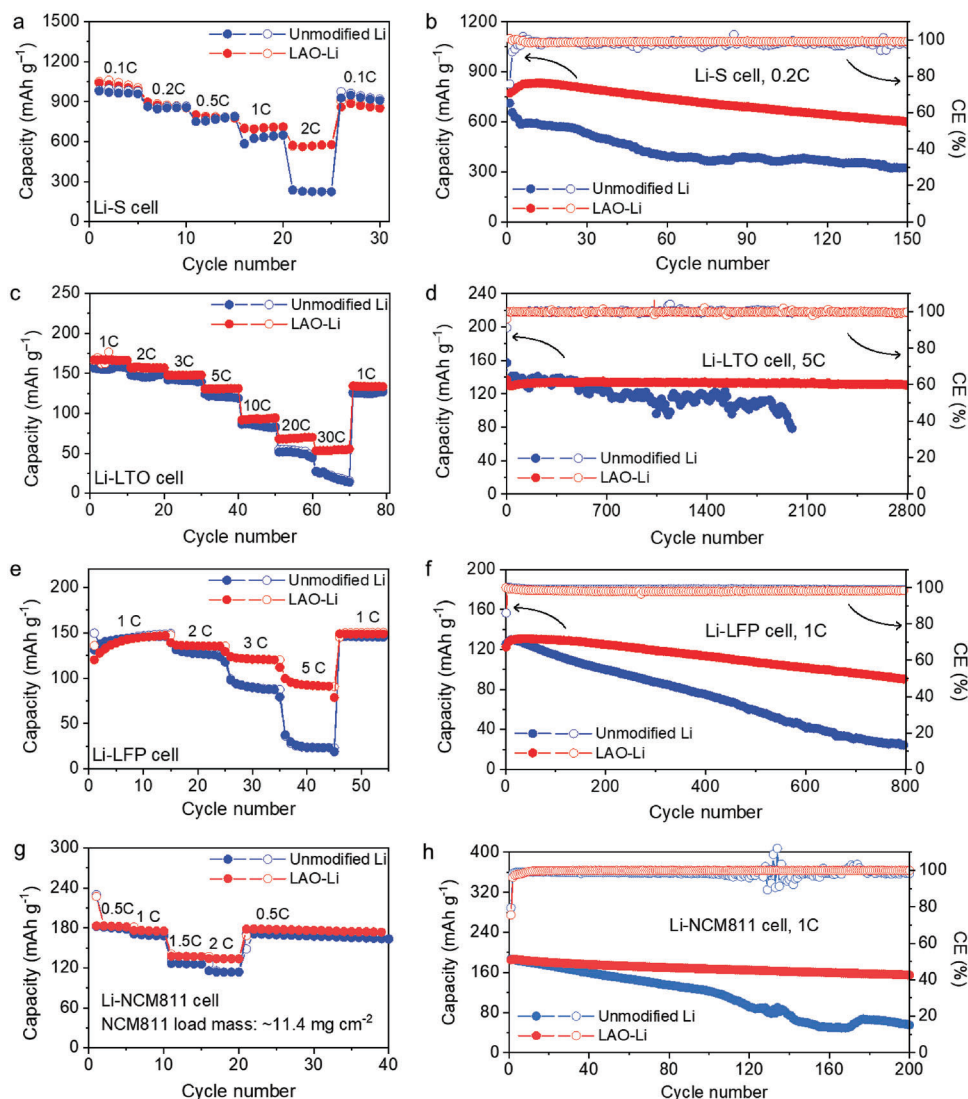


Figure 5. a) Rate performance and b) cycling performance at 0.2C of the Li-S cells with the unmodified Li or LAO-Li anodes. For the Li-S cells, the current of 1C is 1200 mA g⁻¹. c) Rate performance and d) cycling performance at 5C of the Li-LTO cells with the unmodified Li or LAO-Li anodes. For the Li-LTO cells, the current of 1C is 170 mA g⁻¹. e) Rate performance and f) cycling performance at 1C of the Li-LFP cells with the unmodified Li or LAO-Li anodes. For the Li-LFP cells, the current of 1C is 170 mA g⁻¹. g) Rate performance and h) cycling performance at 1C of the Li-NCM811 cells with the unmodified Li or LAO-Li anodes, the current of 1C is 220 mA g⁻¹.

Supporting Information, the LAO-Li||LTO cell can endure an ultrahigh rate up to 30C (1C = 170 mA g⁻¹) and delivers a capacity of 60 mAh g⁻¹ at 30C. In comparison, the unmodified Li||LTO has a capacity of only 31 mAh g⁻¹, which may due to the severe degradation of Li metal anode cycled at a high current. Additionally, the LAO-Li||LTO cell shows excellent ultralong cycling stability with an initial capacity of 131 mAh g⁻¹ and a capacity retention of 99.2% after 2800 cycles (Figure S17, Supporting Information). In contrast, the capacity of the unmodified Li||LTO gradually decreases during cycling and decays to only 76 mAh g⁻¹ with a capacity retention of 56.2% after 2000 cycles.

Furthermore, to verify the cycling stability of LAO-Li anode for the cells using the ester electrolyte, we assembled the Li-LFP cells and Li-NCM811 cell with the electrolyte of 1 M LiPF₆ in EC:

DEC (1: 1, V: V) for tests. For the rate performance, the LAO-Li||LFP cell shows a similar discharge capacity of 148 mAh g⁻¹ with that of the unmodified Li||LFP cell at 1C, while remains a much higher capacity of 92.8 mAh g⁻¹ than that of the unmodified Li||LFP cell (only 25.0 mAh g⁻¹) at 5C (Figure S18, Supporting Information). Also, the LAO-Li||LFP cell exhibits better cycling performance than that of the unmodified Li||LFP cell at a rate of 1C (Figure S19). After 800 cycles, LAO-Li||LFP cell has a remaining capacity of 91 mAh g⁻¹, while pristine Li||LFP cell has only 24 mAh g⁻¹, and the charge-discharge profiles of LAO-Li||LFP cell maintain stable (Figure S19, Supporting Information). We further tested the full cells with LFP and NCM811 cathodes at a higher active mass loading. The load mass of LFP cathode was ≈15.1 mg cm⁻², therefore, the Li-LFP full cells tested at 1C (i.e., 2.2 mA cm⁻²). The high-load LAO-Li||LFP cells exhibit

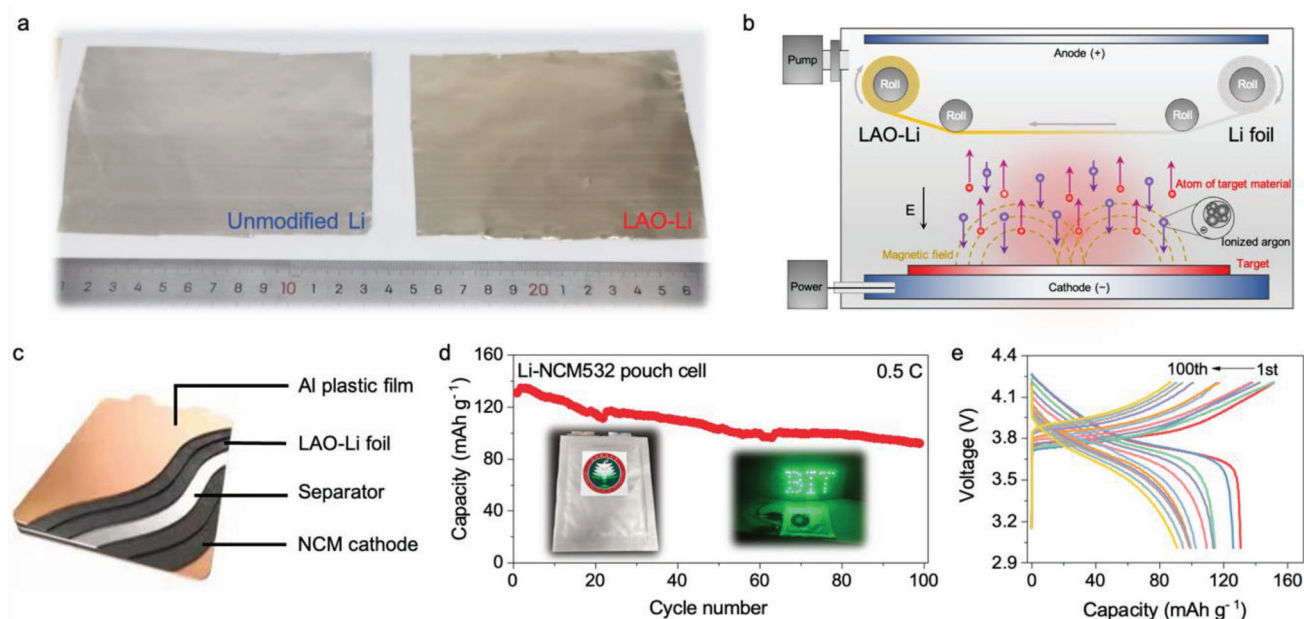


Figure 6. a) Photographs of the unmodified Li foil (left) and LAO-Li foil (right) with a large size of $\approx 13 \text{ cm} \times 13 \text{ cm}$. b) Continuous roll-to-roll manufacturing schematic of LAO-Li. c) Schematic showing the structure of the pouch cell with the LAO-Li anode and NCM532 cathode and the corresponding d) cycling performance and e) galvanostatic charge/discharge profiles of the cell.

more stable cycling with an initial capacity of 104.2 mAh g^{-1} and remained capacity of 98.1 mAh g^{-1} . In contrast, the unmodified Li||LFP cells with unmodified Li anode only stably cycling for 80 cycles (Figure S20, Supporting Information). For NCM811 cathode with a high load mass of $\approx 11.4 \text{ mg cm}^{-2}$, the electrochemical tests were conducted at a high current density of $\approx 2.5 \text{ mA cm}^{-2}$ at 1C. As the rate performance shown in Figure 5g, the LAO-Li||NCM811 cell exhibits better cycling stability at 1.5 and 2 C. The LAO-Li||NCM811 full cell exhibits an initial capacity of 185.0 mAh g^{-1} , as well as a more stable cycling performance than that of the cell with an unmodified Li anode (Figure 5h).

We suggest that the fabrication of LAO-Li anode is highly scalable. We can easily fabricate the large-size LAO-Li sample (Figure 6a) with a laboratory-grade magnetron sputtering system. In addition, this physical vapor deposition preparation method of thin LAO film on Li foil could be realized using a roll-to-roll process (Figure 6b), and the compatibility of LAO-Li foil with roll-to-roll manufacturing suggests its potential for large-scale production. To further demonstrate the application of LAO-Li anode in practical Li metal batteries, we assemble the LAO-Li||NCM-532 pouch cells for electrochemical measurements (Figure 6c). The mass loading of active materials on the cathode is $\approx 5.5 \text{ mg cm}^{-2}$ and the capacity of the cell is $\approx 3.6 \text{ mAh}$ in the voltage range of 3.0–4.2 V versus Li⁺/Li, which is able to drive the LED devices for a long time (Figure 6d). The LAO-Li anode-based pouch cell shows an initial capacity of 130.9 mAh g^{-1} at 0.5C (1C = 160 mAh g^{-1}) and the capacity can be maintained at 90 mAh g^{-1} after 100 cycles (Figure 6d,e).

3. Conclusion

In this work, we construct a controllable dual-layered SEI in a scalable and low-cost manner to improve the performance of Li

metal batteries. The SEI is self-induced by the predeposited LAO layer during the initial cycles, in which the LAO acts as the inner inorganic layer, and the outer organic layer is produced due to the electrons tunneling through LAO, resulting in the reduction of electrolyte. The robust inner LAO layer can effectively suppress the Li dendrite growth and lead to uniform Li deposition because of its favorable mechanical strength and ionic conductivity. Meanwhile, the outer organic layer can further improve the stability of the interphase between the lithium metal anode and electrolyte. Benefiting from the remarkable effects of this dual-layered SEI, the Li symmetric cell with LAO-Li electrodes exhibits excellent long-term cycling stability. It maintains a low overpotential up to 1800 h at a current density of 1 mA cm^{-2} and an areal capacity of 1 mAh cm^{-2} . The superior electrochemical performance of the LAO-Li anode is also demonstrated in full cells with sulfur, NCM811, ITO, and LFP cathodes. Additionally, the fabrication of LAO-Li anode is highly scalable. A large-size LAO-Li sample can be easily obtained even with a laboratory-grade magnetron sputtering system and this method shows huge potential for large-scale production using a roll-to-roll process. We believe that the design and preparation of LAO-Li anode with self-induced dual-layered SEI provides promising support for the commercialization of LMB.

4. Experimental Section

Fabrication of LAO-Li Anode: Magnetron sputtering system (Shenyang Pengcheng Vacuum Technology Company) was utilized to construct the LAO thin film on the surface of Li metal foil (China Energy Lithium Co., Ltd.). The target material of ultrapure LiAlO₂ (ZhongNuo Advanced Material (Beijing) Technology Co., Ltd.), the sputtering power of 80 W, the working pressure of 1.0 Pa in pure Ar atmosphere, and the distance between the target material and Li metal

foils of 7 cm were used. Notably, due to the high reactivity of the Li metal, all of the magnetron sputtering equipment was connected and placed in the glove box filled with an inert atmosphere for the fabrication process.

Material Characterization: FE-SEM with EDS (Hitachi S4800, Japan), XPS (ULVAC-PHI, PHI QUANTERA-II SXM, Japan), and Optical Microscope (Leica Microsystems, Germany) were used to observe the morphology and chemical composition of different lithium foils. AFM (Bruker, Dimension Icon, US) was used to observe the morphology and measure the elasticity modulus of lithium foils. Cells that after an electrochemical test were disassembled in a glove box with pure argon atmosphere. Then the surface of Li anode electrodes was washed several times using Dimethyl carbonate. Finally, the washed Li anode electrodes were dried in an argon atmosphere. After washing, the X-ray photoelectron spectroscopy (XPS) measurements were carried out with a Thermo escalab 250XI spectrometer using a monochromatic Al K α X-ray source. The etching rate of Ar⁺ sputtering the Li anodes surface was 5 nm per minutes. ToF-SIMS (PHI nano ToF II, ULVAC-PHI) was also used to investigate the SEI components on Cu current collector. A special transfer vessel, which can directly transfer the sample from the glovebox to the vacuum chamber of ToF-SIMS, was used for sample transfer without being exposed to ambient air. The sputter etching was performed using an Ar⁺ beam (3 kV, 100 nA) to obtain a depth profile. The area of analysis is 100 $\mu\text{m} \times 100 \mu\text{m}$, while the sputtering area is 400 $\mu\text{m} \times 400 \mu\text{m}$. The elements distribution on the surface of SEI under high resolution was recorded by a 2100 plus transmission electron microscope (TEM, JEOL Ltd.) working at 120 kV with an Elsa cryo-transfer station. Li metal was deposited on a Cu grid with a capacity of 0.5 mAh cm⁻² deposited at 0.2 mA cm⁻². Then the Cu grid was soaked in DME. In the cryo-TEM test, the Cu grid or microgrid was directly mounted to the holder (Gatan 698, cryo-transfer holder) and maintained at a low temperature of -170 °C.

Electrochemical Measurement: Coin cells (CR2025, Canrd) were assembled in the argon-filled glove box (Mikrouna, China). Corrtest electrochemical workstations were used for the impedance measurements with a frequency range of 10–10⁵ Hz and an amplitude of 5 mV. Battery testers (CT-4008T, Neware, China) were used for the galvanostatic measurements at room temperature. The pristine Li foils with a thickness of 100 μm and the fabricated LAO-Li foils were cut into the discs with a diameter of 16 μm . Celgard 2300 (PP/PE/PP, Canrd) was used as a separator with a diameter of 19 μm . The electrolyte used in the symmetric cells was the mixture solvent of DOL: DME (1: 1 in volume) with 1 M LiTFSI and 0.1 M LiNO₃. Then the LAO-modified Cu foils were cut into the discs with a diameter of 16 μm and used in Li-Cu half cells. Li-Cu cells were measured at a current density of 1.0 mA cm⁻² with an areal capacity of 1.0 mAh cm⁻² and a cut-off voltage of 3.0 V for the Li-stripping process.

For the full cells, CR2025 coin cells were assembled with LAO-Li or unmodified Li as anodes, and LiFePO₄ (LFP), sulfur, LiNi_{0.8}Co_{0.1}Mn_{0.1}O₂ (NCM811) or Li₄Ti₅O₁₂ (LTO) as cathodes, respectively. The cathodes were fabricated using slurry with 80% active materials, 10% polyvinylidene fluoride (PVDF), and 10% carbon black coated on the aluminum foil, and dried at 80 °C for 24 h before use. All the cathodes were cut into electrodes with a diameter of 11 μm . The active material mass loadings were ≈ 5.3 and 15.1 mg cm⁻² for LFP, ≈ 3 mg cm⁻² for sulfur, ≈ 11.4 mg cm⁻² for NCM811, ≈ 7 mg cm⁻² for LTO. The Li-LFP and Li-NCM811 full cells used 1 M LiPF₆ in EC: DEC (1: 1, V: V) as the electrolyte and were tested in the voltage range of 2.4–3.8 V (versus Li⁺/Li). The Li-S full cells used 1 M LiTFSI in DOL: DME (1: 1, V: V) with the additive of 0.1 M LiNO₃ as the electrolyte and were tested in the voltage range of 1.6–2.7 V (versus Li⁺/Li). The Li-LTO full cells used 1 M LiTFSI in DOL: DME (1: 1, V: V) with the additive of 0.1 M LiNO₃ as the electrolyte and were tested in the voltage range of 1.0–3.0 V (versus Li⁺/Li).

For the pouch cells, the area of the cathode electrode was ≈ 5 cm² and the areal load of active material was 5.5 mg cm⁻², used 1 M LiPF₆ in EC: DEC (1: 1, V: V) as the electrolyte and were tested in the voltage range of 3.0–4.2 V (vs. Li⁺/Li). The pouch cells were assembled and sealed in glove box with an argon atmosphere.

Supporting Information

Supporting Information is available from the Wiley Online Library or from the author.

Acknowledgements

X.H. and Y.M. contributed equally to this work. This work was supported by the National Natural Science Foundation of China (52002024), the National Key R&D Program of China (2021YFB3800300), the Beijing Outstanding Young Scientists Program (BJJWZYJH01201910007023), the Young Elite Scientists Sponsorship Program by CAST (2022QNRC001), the Xiaomi Innovation Joint Fund of Beijing Municipal Natural Science Foundation (L223012), the Key Scientific and Technological Innovation Project of Shandong (2022CXGC020301), and the Distinguished Young Scholars of the Shandong Provincial Natural Science Foundation (Overseas) (2023HWYQ-112).

Conflict of Interest

The authors declare no conflict of interest.

Data Availability Statement

The data that support the findings of this study are available from the corresponding author upon reasonable request.

Keywords

lithium metal anode, lithium deposition, solid electrolyte interphase, dual-layered SEI, LiAlO₂

Received: April 20, 2023

Revised: August 3, 2023

Published online:

- 1) a) P. G. Bruce, S. A. Freunberger, L. J. Hardwick, J.-M. Tarascon, *Nat. Mater.* **2012**, 11, 19; b) X.-B. Cheng, C.-Z. Zhao, Y.-X. Yao, H. Liu, Q. Zhang, *Chem* **2019**, 5, 74; c) D. Bruce, K. Hareesh, J.-M. Tarascon, *Science* **2011**, 334, 928.
- 2) a) M. Armand, J. M. Tarascon, *Nature* **2008**, 451, 652; b) T. JM. A. M., *Nature* **2001**, 414, 359.
- 3) a) J. Qian, Y. Xing, Y. Yang, Y. Li, K. Yu, W. Li, T. Zhao, Y. Ye, L. Li, F. Wu, R. Chen, *Adv. Mater.* **2021**, 33, 2100810; b) W. J. Qu, M. X. Yan, R. Luo, J. Qian, Z. Y. Wen, N. Chen, L. Li, F. Wu, R. J. Chen, *J. Power Sources* **2021**, 484, 229195; c) J. Qian, F. Wang, Y. Li, S. Wang, Y. Zhao, W. Li, Y. Xing, L. Deng, Q. Sun, L. Li, F. Wu, R. Chen, *Adv. Funct. Mater.* **2020**, 30, 2000742; d) F. Wang, J. Qian, Y. Li, K. Yu, L. Li, F. Wu, R. Chen, *ACS Appl. Mater. Interfaces* **2020**, 12, 21701.
- 4) F. Shi, A. Pei, D. T. Boyle, J. Xie, X. Yu, X. Zhang, Y. Cui, *Proc. Natl. Acad. Sci. USA* **2018**, 115, 8529.
- 5) a) A. C. Kozen, C.-F. Lin, A. J. Pearse, M. A. Schroeder, X. Han, L. Hu, S.-B. Lee, G. W. Rubloff, M. Noked, *ACS Nano* **2015**, 9, 5884; b) Y. He, Y. Zhang, Z. Wang, X. Li, Z. Lü, X. Huang, Z. Liu, *Adv. Funct. Mater.* **2021**, 31, 2101737.
- 6) J. Zhao, L. Liao, F. Shi, T. Lei, G. Chen, A. Pei, J. Sun, K. Yan, G. Zhou, J. Xie, C. Liu, Y. Li, Z. Liang, Z. Bao, Y. Cui, *J. Am. Chem. Soc.* **2017**, 139, 11550.

- [7] a) Q. Xu, J. Lin, C. Ye, X. Jin, D. Ye, Y. Lu, G. Zhou, Y. Qiu, W. Li, *Adv. Energy Mater.* **2019**, *10*, 1903292; b) N. Li, K. Zhang, K. Xie, W. Wei, Y. Gao, M. Bai, Y. Gao, Q. Hou, C. Shen, Z. Xia, B. Wei, *Adv. Mater.* **2020**, *32*, 1907079.
- [8] a) J. Qian, Y. Li, M. Zhang, R. Luo, F. Wang, Y. Ye, Y. Xing, W. Li, W. Qu, L. Wang, L. Li, Y. Li, F. Wu, R. Chen, *Nano Energy* **2019**, *60*, 866; b) K. Yu, J. Qian, F. Wang, X. Guo, L. Li, F. Wu, R. Chen, *ACS Appl. Energy Mater.* **2021**, *4*, 11878; c) Y. Xu, L. Gao, L. Shen, Q. Liu, Y. Zhu, Q. Liu, L. Li, X. Kong, Y. Lu, H. B. Wu, *Matter* **2020**, *3*, 1685.
- [9] a) D. Luo, L. Zheng, Z. Zhang, M. Li, Z. Chen, R. Cui, Y. Shen, G. Li, R. Feng, S. Zhang, G. Jiang, L. Chen, A. Yu, X. Wang, *Nat. Commun.* **2021**, *12*, 186; b) C. Yan, X. B. Cheng, Y. X. Yao, X. Shen, B. Q. Li, W. J. Li, R. Zhang, J. Q. Huang, H. Li, Q. Zhang, *Adv. Mater.* **2018**, *30*, 1804461; c) C. Yan, X. B. Cheng, Y. Tian, X. Chen, X. Q. Zhang, W. J. Li, J. Q. Huang, Q. Zhang, *Adv. Mater.* **2018**, *30*, 1707629.
- [10] a) M. Wan, S. Kang, L. Wang, H.-W. Lee, G. W. Zheng, Y. Cui, Y. Sun, *Nat. Commun.* **2020**, *11*, 829; b) D. Lee, S. Sun, J. Kwon, H. Park, M. Jang, E. Park, B. Son, Y. Jung, T. Song, U. Paik, *Adv. Mater.* **2020**, *32*, 1905573; c) S. Luo, Z. Wang, X. Li, X. Liu, H. Wang, W. Ma, L. Zhang, L. Zhu, X. Zhang, *Nat. Commun.* **2021**, *12*, 6968; d) Y. Ma, L. Wang, S. Fu, R. Luo, W. Qu, X. Hu, R. Chen, F. Wu, L. Li, *J. Mater. Chem. A* **2020**, *8*, 23574; e) Y. Ma, L. Li, L. Wang, J. Qian, X. Hu, W. Qu, Z. Wang, R. Luo, S. Fu, F. Wu, R. Chen, *ACS Appl. Mater. Interfaces* **2020**, *12*, 31411.
- [11] a) M. S. Kim, Z. Zhang, P. E. Rudnicki, Z. Yu, J. Wang, H. Wang, S. T. Oyakhire, Y. Chen, S. C. Kim, W. Zhang, D. T. Boyle, X. Kong, R. Xu, Z. Huang, W. Huang, S. F. Bent, L. W. Wang, J. Qin, Z. Bao, Y. Cui, *Nat. Mater.* **2022**, *21*, 445; b) Y. Yang, D. M. Davies, Y. Yin, O. Borodin, J. Z. Lee, C. Fang, M. Olguin, Y. Zhang, E. S. Sablina, X. Wang, C. S. Rustomji, Y. S. Meng, *Joule* **2019**, *3*, 1986; c) F. Wu, J. Qian, R. Chen, J. Lu, L. Li, H. Wu, J. Chen, T. Zhao, Y. Ye, K. Amine, *ACS Appl. Mater. Interfaces* **2014**, *6*, 15542; d) D. J. Lee, H. Lee, Y. J. Kim, J. K. Park, H. T. Kim, *Adv. Mater.* **2016**, *28*, 857.
- [12] a) O. Borodin, J. Self, K. A. Persson, C. Wang, K. Xu, *Joule* **2020**, *4*, 69; b) X. Cao, H. Jia, W. Xu, J.-G. Zhang, *J. Electrochem. Soc.* **2021**, *168*, 010522.
- [13] a) W. Liu, P. Liu, D. Mitlin, *Adv. Energy Mater.* **2020**, *10*, 2070177; b) M. D. Tikekar, S. Choudhury, Z. Tu, L. A. Archer, *Nat. Energy* **2016**, *1*, 16114.
- [14] a) C. Yan, X.-B. Cheng, Y. Tian, X. Chen, X.-Q. Zhang, W.-J. Li, J.-Q. Huang, Q. Zhang, *Adv. Mater.* **2018**, *30*, 1707629; b) Y. Zhao, M. Amirmaleki, Q. Sun, C. Zhao, A. Codireni, L. V. Goncharova, C. Wang, K. Adair, X. Li, X. Yang, F. Zhao, R. Li, T. Filletter, M. Cai, X. Sun, *Matter* **2019**, *1*, 1215.
- [15] X.-B. Cheng, C. Yan, X.-Q. Zhang, H. Liu, Q. Zhang, *ACS Energy Lett.* **2018**, *3*, 1564.
- [16] Y. Ma, L. Li, J. Qian, W. Qu, R. Luo, F. Wu, R. Chen, *Energy Storage Mater.* **2021**, *39*, 203.
- [17] a) B. Singh, M. K. Gupta, R. Mittal, S. L. Chaplot, *Phys. Chem. Chem. Phys.* **2018**, *20*, 12248; b) T. Amriou, A. Sayede, B. Khelifa, C. Mathieu, H. Aourag, *J. Power Sources* **2004**, *130*, 213; c) F. Cheng, Y. Xin, Y. Huang, J. Chen, H. Zhou, X. Zhang, *J. Power Sources* **2013**, *239*, 181; d) J. Li, S. Luo, X. Ding, Q. Wang, P. He, *ACS Appl. Mater. Interfaces* **2018**, *10*, 10786; e) M. M. Islam, T. Bredow, *J. Phys. Chem. Lett.* **2015**, *6*, 4622.
- [18] Y. Liu, X. Xu, O. O. Kapitanova, P. V. Evdokimov, Z. Song, A. Matic, S. Xiong, *Adv. Energy Mater.* **2022**, *12*, 2103589.
- [19] L. Zhang, T. Yang, C. Du, Q. Liu, Y. Tang, J. Zhao, B. Wang, T. Chen, Y. Sun, P. Jia, H. Li, L. Geng, J. Chen, H. Ye, Z. Wang, Y. Li, H. Sun, X. Li, Q. Dai, Y. Tang, Q. Peng, T. Shen, S. Zhang, T. Zhu, J. Huang, *Nat. Nanotechnol.* **2020**, *15*, 94.
- [20] A. Mauger, M. Armand, C. M. Julien, K. Zaghib, *J. Power Sources* **2017**, *353*, 333.
- [21] Y. Li, W. Huang, Y. Li, A. Pei, D. T. Boyle, Y. Cui, *Joule* **2018**, *2*, 2167.
- [22] B. D. Adams, J. Zheng, X. Ren, W. Xu, J. G. Zhang, *Adv. Energy Mater.* **2017**, *8*, 1702097.